Structure and Dynamics of the Second and Third Transmembrane Domains of Human Glycine Receptor[†,‡]

Dejian Ma,[§] Zhanwu Liu,[§] Ling Li,[§] Pei Tang,[§,||] and Yan Xu*[,§,||]

Department of Anesthesiology and Department of Pharmacology, University of Pittsburgh School of Medicine, Pittsburgh, Pennsylvania 15261

Received February 10, 2005; Revised Manuscript Received April 25, 2005

ABSTRACT: A 61-residue polypeptide resembling the second and third transmembrane domains (TM23) of the α-1 subunit of human glycine receptor and its truncated form, both with the wild-type loop linking the two TM domains (the "23" loop), were studied using high-resolution NMR. Well-defined domain structures can be identified for the TM2, 23 loop, and TM3 regions. Contrary to the popular model of a long and straight α-helical structure for the pore-lining TM2 domain for the Cys-loop receptor family, the last three residues of the TM2 domain and the first eight residues of the 23 loop (S16−S26) seem to be intrinsically nonhelical and highly flexible even in trifluoroethanol, a solvent known to promote and stabilize α-helical structures. The six remaining residues of the 23 loop and most of the TM3 domain exhibit helical structures with a kinked π-helix (or a π-turn) from W34 to C38 and a kink angle of 159 ± 3°. The tertiary fold of TM3 relative to TM2 is defined by several unambiguously identified long-range NOE cross-peaks within the loop region and between TM2 and TM3 domains. The 20 lowest-energy structures show a left-handed tilt of TM3 relative to TM2 with a tilting angle of 44 ± 2° between TM2 (V1−Q14) and TM3 (L39−E48) helix axes. This left-handed TM2−TM3 arrangement ensures a neatly packed right-handed quaternary structure of five subunits to form an ion-conducting pore. This is the first time that two TM domains of the glycine receptor linked by the important 23 loop have ever been analyzed at atomistic resolution. Many structural characteristics of the receptor can be inferred from the structural and dynamical features identified in this study.

Glycine receptor (GlyR)[1] belongs to a superfamily of neurotransmitter-gated, postsynaptic receptors that are responsible for fast synaptic transmission. This superfamily also includes nicotinic acetylcholine receptor (nAChR), type A and type C γ-aminobutyric acid ($GABA_A$ and $GABA_C$, respectively) receptors, type 3 serotonin 5-hydroxytryptamine ($5\text{-}HT_3$) receptor, and the invertebrate glutamate and histidine receptors. All members in the superfamily are collectively known as the "Cys-loop" receptors because they contain pairs of disulfide-bonded cysteines, separated by 13 amino acid residues (*1*), in the N-terminal extracellular domain near the membrane interface (*2*). It is believed that the Cys loop is coupled to the transmembrane (TM) domains for allosteric control of ion channel gating.

The structural data for the Cys-loop receptors are derived mostly from studies of the muscle-type nAChR because of its abundance in the electric organ of the electric fish. All Cys-loop receptors are believed to function as pentameric oligomers composed of five subunits, each consisting of a large extracellular N-terminal domain, four TM domains termed TM1−TM4, and a large intracellular loop between TM3 and TM4. Recently, the structure of a soluble acetylcholine-binding protein (AChBP) was determined by X-ray crystallography to atomic resolution (*3*). Because the sequence of AChBP is ∼20−24% identical to the aligned extracellular domain sequence of nAChR, and 15−18% identical to the aligned extracellular domain sequences of glycine, $GABA_A$, $GABA_C$, and $5\text{-}HT_3$ receptor subunits, the AChBP structure provides a structural template for the extracellular domains of the Cys-loop receptors.

Studies of the TM domain structures have lagged behind. Despite the continuing efforts by many investigators in the past two decades, there are currently no atomic-resolution, full TM domain structures available for any members of the Cys-loop receptors. Ideally, one would hope that a high-resolution structure of all the TM domains can be solved as one piece. This is only partially achieved in a recent TM structural model of the muscle-type nAChR, derived from the cryo-electron microscopy (cryo-EM) data with the phase terms significant at 4 Å (*4*). Although the side chain information is lacking at ≥4 Å resolution, the cryo-EM

[†] This work was supported in part by grants from the National Institutes of Health (R37GM049202 and R01GM069766 to Y.X. and R01GM66358 to P.T.).

[‡] Coordinates have been deposited as Protein Data Bank entry 1ZHD.

* To whom correspondence should be addressed: W-1358 Biomedical Science Tower, University of Pittsburgh School of Medicine, Pittsburgh, PA 15261. Telephone: (412) 648-9922. Fax: (412) 648-9587. E-mail: xuy@anes.upmc.edu.

[§] Department of Anesthesiology.

[||] Department of Pharmacology.

[1] Abbreviations: GlyR, glycine receptor; TM23, transmembrane domains 2 and 3 of the human GlyR α_1 subunit; TFE, trifluoroethanol; DPC, dodecylphosphocholine; DMPC, dimyristoylphosphatidylcholine; NMR, nuclear magnetic resonance; R_1 and R_2, longitudinal and transverse relaxation rate constants, respectively; NOE, nuclear Overhauser effect; 2D, two-dimensional; 3D, three-dimensional; NOESY, NOE spectroscopy; TOCSY, total correlation spectroscopy; HSQC, heteronuclear single-quantum coherence; τ_m, global rotational correlation time; S^2, squared order parameter; R_{ex}, exchange rate constant; τ_e, effective correlation time for fast internal motions; CD, circular dichroism.

10.1021/bi050256n CCC: $30.25
Published on Web 05/27/2005

structural approximation of the polytopic TM domains nevertheless provides the basis for other complementary high-resolution approaches, including the domain-by-domain approach by high-resolution NMR (*5*−*7*), in such a way that the high-resolution domain structures can be superimposed onto the cryo-EM structural template.

The theoretical ground for the reductionist NMR approach is that the TM domain folding and oligomerization can be conceptualized as involving two energetically distinct stages (*8*). Experimentally, this would mean that if the TM domains are *properly truncated*, then the secondary structure is governed by the membrane-mimetic environments and the tertiary and quaternary associations of the domains are controlled by the interactions among side chains and between side chains and lipids. The validity of this approach for polytopic helical structures of large integral proteins has been tested recently for bacteriorhodopsin and lactose permease of *Escherichia coli* (lac Y). Comparisons are made for the structures derived from the NMR constraints obtained on the truncated TM segments in organic solvents to the known X-ray structures of these membrane proteins (*9*, *10*). The striking agreement between the NMR structures and the corresponding domains in the X-ray structures, particularly with the rmsd values of superposition as small as 1.4−2.1 Å for helix−turn−helix motifs, suggests that NMR studies of truncated TM domains can provide complementary atomic-resolution structural information that cannot be obtained by any other existing methods.

Within the same conceptual framework, we have determined the TM domain structures of the human neuronal GlyR. We report here the first high-resolution TM2−TM3 (TM23) structure of the GlyR α1 subunit in trifluoroethanol (TFE). TFE was chosen not only to achieve a high spectral resolution but also to create the most favorable helix-promoting conditions to verify the high helical content in the recently proposed nAChR TM structural model, which seems to disagree with several earlier experimental studies (*11*−*14*).

MATERIALS AND METHODS

Protein Expression. TM23 segments of desired lengths were expressed using the Novagen pET-31b(+) system (Novagen, Milwaukee, WI) by fusing the target peptide genes between an upstream 125-amino acid ketosteroid isomerase (KSI) gene and a downstream His-tag sequence for high-yield expression and purification. The forward and reverse primers were synthesized, purified, and phosphorylated by Genosys (Fisher Scientific), and the cDNA of the human GlyR α1 subunit was used as a template for the PCR amplification of the selected TM segments. To avoid internal cleavage by CNBr after protein expression, a standard protocol was used to mutate two internal methionines in α1-TM23 to leucine, which is the corresponding amino acid at the same positions in the wild-type β form of GlyR. *E. coli* BL21(DE3)pLysS competent cells (Novagen) were used for expression either in LB medium (containing 10 g/L tryptone peptone, 5 g/L yeast extract, 5 g/L NaCl, and 100 μg/mL ampicillin) or in M9 medium (containing 7 g/L Na_2HPO_4, 3 g/L KH_2PO_4, 1 g/L $(NH_4)_2SO_4$, 50 mg/L thiamine, 5 g/L glucose, 1 mM $MgSO_4$, 0.1 mM $CaCl_2$, 0.5 g/L NaCl, and 100 μg/mL ampicillin). The latter contained $(^{15}NH_4)_2SO_4$ and [U-^{13}C]glucose (Cambridge Isotope Labs, Andover, MA) as the sole sources of ^{15}N and ^{13}C, respectively.

After expression, the KSI−TM23 fusion proteins were extracted from the inclusion bodies in two lysis steps and then purified on staggered His-Bind chromatography columns (Novagen). The cleavage of the TM23 segments from the fusion protein was achieved using the standard protocol (*15*) in the presence of CNBr (30−80 mg per 10 mg of protein) in 70% trifluoroacetic acid. Final TM23 purification was carried out using reverse-phase HPLC with an analytical C4 column (Vydac, Hesperia, CA).

Two different lengths of the TM23 segment of the GlyR α1 subunit were studied. One spans the putative TM2 and TM3 domains along with the "23" loop, as predicted from the amino acid hydropathy. The wild-type sequence of full-length TM23 is LPARVGLGITTVLTMTTQSSGSRASLP-KVSYVKAIDIWMAVCLLFVFSALLEYAAVNFVSRX, where the TM2 and TM3 domains are underlined, and X (=KKKKHRLLEHHHHHH) is attached for the purpose of increasing the solubility and easy purification. In the other truncated version of TM23 (*16*), the last nine amino acids and X in the above sequence were truncated and replaced with the His tag (QMLLEHHHHHH). Using the relative numbering convention (*6*, *17*), the first arginine in the sequence (R252) is designated R0′.

CD Spectroscopy. The CD spectra of GlyR TM23 in the wavelength range from 185 to 290 nm were acquired at room temperature using a cuvette with a path length of 1 mm on an Aviv CD spectrometer (model 202, Aviv Instruments, Lakewood, NJ). The wavelength step was 1 nm with an averaging time of 1 s. The spectra after solvent subtraction were analyzed using the Web-based CD analysis software DICHROWEB at www.cryst.bbk.ac.uk/cdweb/html/home.html (*18*).

NMR Experiments. NMR samples were prepared as previously described (*6*, *7*, *19*). The protein concentration was typically 1 mM in TFE-d_2 (CF_3CD_2OH). The NMR experiments were conducted at 30 °C on a Bruker Avance 600 MHz spectrometer (Bruker Instruments, Billerica, MA), equipped with a TCI cryoprobe and an inverse-detection triple-resonance TXI probe, and on a Chemagnetics CMXW 400 MHz spectrometer (Varian NMR Inc., Fort Collins, CO), equipped with an inverse-detection double-resonance Z-Spec probe (Nalorec Cryogenics Co., Martinez, CA).

Sequential assignment was carried out using a series of 2D and 3D experiments, including TOCSY, NOESY, HNCA, and HNCO. The ^{1}H-^{15}N heteronuclear single-quantum correlation (HSQC) spectra were acquired in 1024 (^{1}H) × 120 (^{15}N) complex points, with a spectral width of 12 ppm for ^{1}H, a spectral width of 40 ppm for ^{15}N, and 16 transients for each time increment. The ^{15}N-decoupled ^{1}H homonuclear 2D NOESY and TOCSY spectra were acquired in 2048 × 512 complex points, with a ^{1}H spectral width of 12 ppm and 32 or 64 transients for each time increment. In almost all cases, the mixing time was 100−150 ms for 2D NOESY and 60 ms for TOCSY. In one 2D NOESY experiment, where the sole purpose is to confirm or exclude ambiguous long-range NOEs and not to measure cross-peak intensities, the mixing time was extended to 300 ms. The 3D NOESY-HSQC spectrum (mixing time of 150 ms) was acquired in 2048 (^{1}H) × 40 (^{15}N) × 200 (^{1}H) complex points, with spectral widths of 14 and 40 ppm for ^{1}H and ^{15}N,

respectively, and 16 transients for each time increment. A Watergate pulse scheme (*20*) was applied for the suppression of the solvent peak. The States-TPPI method (*21*) was used for quadrature detection in the indirect dimensions. HNCO and HNCA spectra were acquired with 1024 (^{1}H) × 40 (^{15}N) × 128 (^{13}C) data points. Echo-antiecho and States-TPPI methods were used for quadrature detection in ^{15}N and ^{13}C dimensions, respectively. The observed ^{1}H chemical shift was referenced to the internal DSS standard at 0 ppm. The ^{15}N and ^{13}C chemical shifts were indirectly referenced (*22*).

Dynamics Measurements. The longitudinal and transverse relaxation rate constants, R_1 and R_2, and the steady-state ^{15}N-{^{1}H} NOE of the backbone amide ^{15}N were measured at 30 °C on both the 600 and 400 MHz spectrometers using the standard pulse sequences (*23*). The R_1 and R_2 measurements were collected using a 2 s relaxation delay. The R_1 data were typically recorded using 10 delay values: 20, 50, 100, 170, 300, 500, 750, 1000, 1250, and 1500 ms. The R_2 data were typically recorded using eight delay values: 16.71, 33.42, 50.13, 66.84, 83.55, 100.26, 116.97, and 133.68 ms. The steady-state ^{15}N{^{1}H} NOE experiments were carried out with and without ^{1}H saturation in an interleave fashion. The saturation of protons was achieved by a train of 120° high-power pulses separated by 5 ms for 3 s.

Proton−Deuteron Exchange Measurements. The exchange of the amide protons with the deuterons in the solvent (H−D exchange) was assessed on the 400 MHz instrument at 30 °C. The NMR samples were prepared by dissolving TM23 in 100% TFE-d_3 (CF_3CD_2OD). The ^{1}H−^{15}N HSQC experiments were carried out immediately and in 2 h intervals for the first 6 h, and then repeated at 19 and 43 h. The exchange rates for the backbone amide protons are classified semi-quantitatively as very slow (>50% intensity remaining after 43 h), slow (>50% at 19 h but <50% at 43 h), intermediate (<50% at 19 h), and fast (<50% after exchange for 6 h). The residues in the very slow and slow categories are considered for hydrogen bonding restraints in the structural refinement (see below).

Data Processing and Analysis. All data were processed using nmrPipe (*24*) and analyzed using PIPP (*25*) or Sparky (*26*). Structures were calculated using XPLOR-NIH (*27*, *28*). Distance restraints derived from 2D NOESY and 3D NOESY-HSQC experiments with mixing time of 100−150 ms were grouped into four categories: 1.8−2.7, 1.8−3.3, 1.8−5.0, and 1.8−6.0 Å for strong, medium, weak, and very weak NOEs, respectively. The initial structural calculations were carried out using only the NOE restraints with the simulated annealing protocol (*29*). Fifty structures with no violations above the threshold conditions of 5° for angles, improper angles, and dihedral angles and 0.05 and 0.5 Å for the bonds and NOEs, respectively, were taken for further analysis. When the H−D exchange data were taken into consideration, the hydrogen bond restraints were included in the further calculation and refinement for residues where the H−D exchange was in the slow or very slow category and at the same time the $d_{\alpha N}(i,i+3)$ or $d_{\alpha\beta}(i,i+3)$ NOE connectivity was present. Each hydrogen bond was converted into two distance restraints: r_{NH-O} (1.9−2.3 Å) and r_{N-O} (2.4−3.0 Å) (*30*). Because we have found that a single-point mutation, S15Y, can induce a specific chemical shift change at A36 (see Figure S1 of the Supporting Information), the C_α and C_β distances between S15 and A36 were weakly restrained in the first refinement step at 8 and 9 Å (*31*), respectively, and then relaxed to 10 Å in the subsequent refinement steps. In the final refinement steps, the dielectric constant of TFE (26.7) was used. Twenty refined structures with the lowest energy were used for analysis.

The ^{15}N relaxation parameters were analyzed by the Lipari−Szabo model-free approach (*32*, *33*), using Model-Free (version 4.15) (*34*). The R_1 and R_2 values were determined from two-parameter fitting of the peak intensities versus the variable delays to a single-exponential function. The ^{15}N{^{1}H} NOE values were obtained as the ratio of the peak intensities measured with and without ^{1}H saturation. The uncertainties for R_1 and R_2 are obtained from the fit of the exponential decay curves. The uncertainties for ^{15}N{^{1}H} NOEs were determined using the relationship based on the background noise levels, as described by Farrow et al. (*23*).

Large-Scale Computer Simulation in DMPC Membrane. To model a pentameric GlyR channel using the high-resolution NMR structure of the TM23 domains, the monomer structure with the lowest energy was docked into a homopentameric complex with 5-fold symmetry along the center axis of the complex. TM2 of the NMR structure was superimposed onto the helical coordinates of the TM2 domain in the 4 Å resolution EM structure (Protein Data Bank entry 1OED) of the nAChR. The TM1 domain was assumed to be helical and homology modeled using TM1 in the same EM structure of the nAChR. Energy minimization of the pentameric complex was performed for 5000 steps with the backbone fixed, 10 000 steps each with 5 and 1 kcal/mol harmonic restraints on the backbone, and 50 000 steps without any restraints. The energy-minimized pentamer was immersed into a pre-equilibrated, fully hydrated palmitoyloleoylphosphatidylcholine (POPC) membrane patch. After 20 000 additional steps of energy minimization of the entire system and 100 ps NVT simulation with a 500 kcal/mol restraint on the protein backbone, over 1 ns NPT simulations were performed with periodical boundary conditions and Particle-Mesh Ewald (PME) for full electrostatic interactions. During NPT simulations, the restraint on the protein backbone was gradually released from 500 to 0 kcal/mol over the first 550 ps. Free NPT dynamics was continued for an additional 500 ps.

RESULTS

Secondary Structures of TM23 As Determined by CD and NMR. Both the full-length and truncated segments of GlyR TM23 exhibit stable structures in TFE. As shown in Figure 1, the structure of TM23 is almost the same in pure TFE and in TFE/water mixtures as long as the TFE concentration is more than 30% (v/v). The helical content of TM23 decreased from 60 to ~50% when the TFE concentration was reduced to 15−20%.

The NMR spectra of TM23 are well-resolved, allowing for complete sequence-specific assignment (Figure 2). For the truncated TM23 segment, only one set of signals was identified, indicating the structural homogeneity in TFE. The full-length TM23 segment also showed only one set of peaks for all residues except G2, L3, G4, and L9, which exhibited an extremely weak minor peak near the noise level. An interesting observation is that the HSQC intensities from some of the peaks in the TM3 domain are relatively weaker

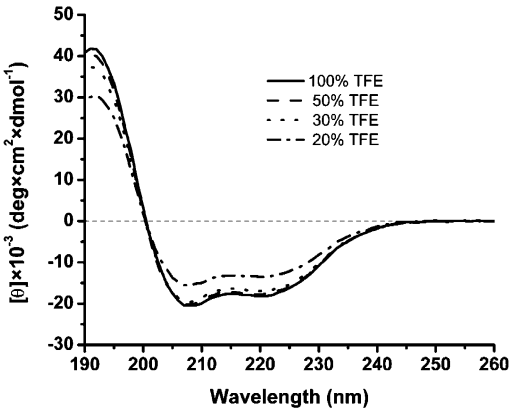

FIGURE 1: Far-UV CD spectra of the TM23 domains of human glycine receptor in various TFE/water mixtures at 25 °C, showing stable and well-defined structures with ~60% α-helical content in solvent mixtures with >30% (v/v) TFE. The α-helical content decreased to ~50% in 20% TFE.

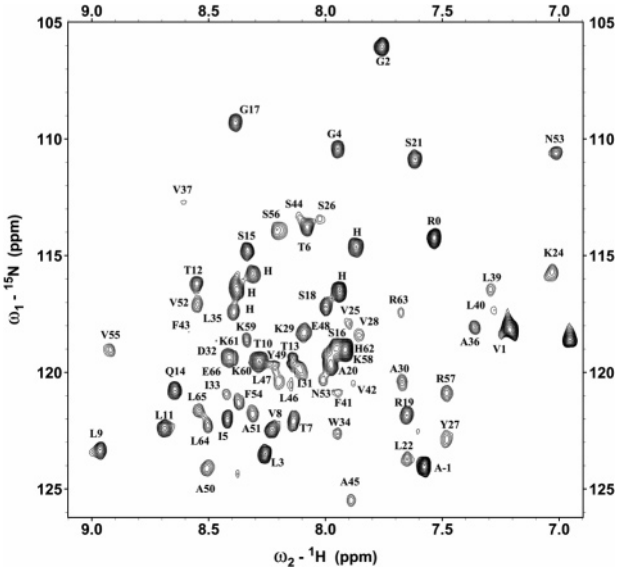

FIGURE 2: Backbone amide proton region of a ^{1}H−^{15}N HSQC spectrum of uniformly ^{15}N-labeled TM23 in TFE-d_2 at 303 K and pH 4.5. Backbone resonance assignments are indicated by the one-letter amino acid code and the sequence number.

than those in the TM2 domain, suggesting the possibility of low-frequency motions in a certain portion of the TM3 domain (*35*). Nevertheless, all peaks are well-defined and resolved with a sufficient signal-to-noise ratio for accurate structural determination.

The sequential and midrange NOE connectivity, the C^α and H^α chemical shift index (CSI), and the H−D exchange results for full-length TM23 are shown in Figure 3. The results for truncated TM23 are essentially the same as for the first 52 residues in Figure 3. The $d_{\alpha\beta}(i,i+3)$ and $d_{\alpha N}(i,i+3)$ NOE connectivity, which is a characteristic of α-helical structure, is present for significant portions of the TM2 and TM3 domains. Such helical characteristics are absent from S16 to S26, a region which encompasses the last three residues of the putative TM2 domain and the first eight residues of the segment traditionally considered as the "23" loop. The H−D exchange results of the backbone amide protons are used to identify the existence of hydrogen bonds. The rates of exchange increased toward the N-terminal residues (from A−1 to G4) and the residues near and within

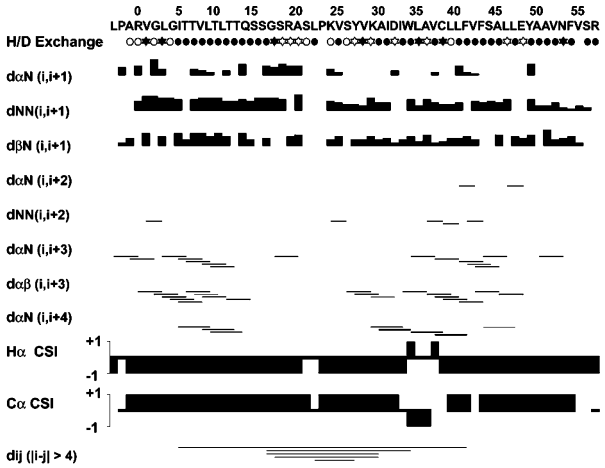

FIGURE 3: Summary of NOE connectivity of TM23 in TFE. Sequential, midrange, and long-range NOE connectivity is linked by line segments with widths proportional to the observed NOE intensities. The chemical shift index for H^α protons and the amide proton exchange with solvent deuterons are also shown. Symbols for the latter are as follows: ●, ★, ☆, and ○ for very slow, slow, intermediate, and fast H−D exchange, respectively.

the 23 loop (S18−Y27). The I5−S16 region showed slow or very slow H−D exchanges, indicating strong hydrogen bonding and a regular α-helical structure. Amide protons from most residues in the TM3 domain showed slow or very slow H−D exchange. Clear exceptions are residues D32, A36, L39, L46, and E48, which exhibit an intermediate or fast H−D exchange, implying a possible deviation from the normal helical structure near these residues.

The CSI displayed in Figure 3 was determined on the basis of the chemical shift differences of the C^α and H^α resonances from the corresponding random-coil values (*36*). W34−V37 exhibited an unusual CSI, providing a preliminary identification of possible abnormality in the secondary structure. We also analyzed the chemical shift pattern of the observed H^N chemical shifts relative to the corresponding values in the random coils. One of the dominating factors of H^N shifts is the exchange with the solvent resonance. Although overall H−D exchange rates are slow in the TM2 domain, slight differences in exchange with the solvent and hence in the intrahelical hydrogen bond strength can be detected from the H^N chemical shift pattern. Figure 4 depicts the differences between the observed H^N chemical shifts and the random-coil values as a function of the residue numbers. Notice the periodical pattern in the TM2 domain. The residues forming the "upward spikes" include L3, I5, V8, L9, L11, T12, Q14, and G17, and the residues at the "downward spikes" are G4, T6, T7, T10, T13, S16, and R19. This pattern nicely matches our earlier prediction of the residues that do or do not line the pore of the GlyR channel (*6*). Most of the residues at the upward spikes have a H^N shift significantly different from the random-coil value, indicating a stronger intrahelical hydrogen bond than that in residues on the opposite side of the helical surface, which is away from the TM3 domain and likely facing the pore when the TM23 segments aggregate into a channel. The H^N shift pattern in the TM3 domain is not as distinct as in the TM2 domain, although a large fluctuation near A36−L40 is clearly noticeable.

High-Resolution NMR Structures of GlyR TM23. Panels A and B of Figure 5 show the structures of the full-length and truncated TM23, respectively. Truncating nine residues

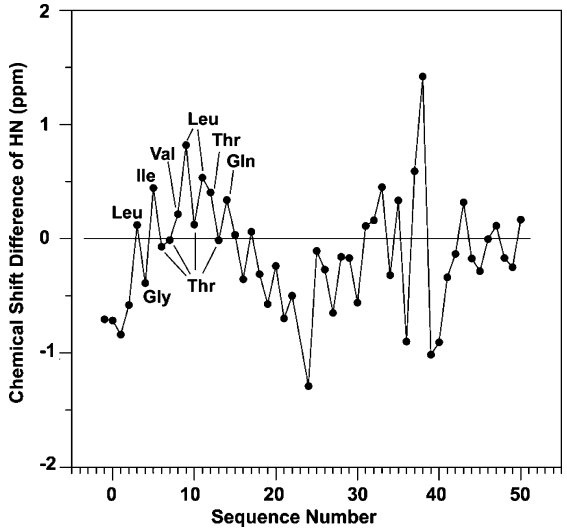

FIGURE 4: Chemical shift differences between the backbone amide proton resonances of the truncated TM23 in TFE and the corresponding values in a random coil are plotted as a function of the sequence number. Notice the periodic pattern of the chemical shift differences in the TM2 domain (see the text for details).

from the C-terminus of TM3 did not significantly alter the tertiary arrangement of TM2 and TM3, confirming that the full-length TM3 helix extends beyond the N-terminus of TM2 in the pseudohairpin fold of TM2 and TM3 domains. The helical structure of the TM2 domain starts from P−2 or A−1 and extends at least to Q14 and at most to S15. The helix leading to the putative TM3 domain starts from Y27 in the second moiety of the 23 loop, is interrupted from W34 to C38, and then continues to the C-terminus. The first half of the loop region between R19 and S26 is less structured and contains a range of conformations, whereas S16−S18, V25, and S26 are likely forming turns. The dynamical nature of the TM23 structure in TFE is shown in panels C−E of Figure 5 for the 20 lowest-energy structures of full-length TM23. The statistics for these and the truncated TM23 structures are given in Table 1. The structures in the TM2 and TM3 domains alone are well defined, with the backbone root-mean-square deviations (rmsds) of the TM2 and TM3 segments alone being only 0.17 ± 0.08 Å (Figure 5C) and 0.10 ± 0.04 Å (Figure 5D), respectively. A large deviation among the 20 structures occurs in the loop region, as the rmsd becomes 0.29 ± 0.09 Å when both TM2 and TM3 domains were fitted. The rmsd increases to 1.18 ± 0.31 Å if the backbone of the entire sequence, including the loop region, is taken into consideration (Figure 5E and Table 1).

The tertiary fold between the TM2 and TM3 domains was refined using several positively identified long-range interhelical NOEs. Unambiguously assigned long-range NOE cross-peaks include pairs from I5H$^{\delta\#}$ to F41H$^{\epsilon\#}$, S16H$^{\beta\#}$ to W34H$^{\eta 2}$, S16H^{N} to A30H$^{\beta\#}$, G17H^{N} to A30H$^{\beta\#}$, and L22H$^{\delta\#}$ to Y27H^{N}. Other possible long-range NOE cross-peaks are either too weak to be detected or ambiguous and are therefore not used in structural calculation and refinement. The 20 lowest-energy structures show a left-handed tilt of TM3 relative to TM2, with a tilting angle of 43.7 ± 2.0° between TM2 (V1−Q14) and TM3 (L39−E48) helix axes. The structures also show that the TM2 helix is slightly curved and the TM3 has a kink near W34 and C38. The kink angle, measured between helix axes of Y27−D32 and L39−E48, is ∼160° (Figure 5F).

Table 1: Statistics of 20 Lowest-Energy Structures of GlyR TM23[a]

	truncated TM23	full-length TM23
no. of distance restraints		
intraresidue ($\|i-j\|=0$)	108	138
sequential ($\|i-j\|=1$)	139	173
medium-range ($2<\|i-j\|\le 4$)	77	92
long-range ($\|i-j\|>4$)[b]	7	7
no. of NOEs per residue	6.1	6.8
no. of H-bond restraints (two per bond)	44	54
total no. of restraints	375	464
no. of refined structures	20	20
energy (kcal/mol)		
E_{NOE}[c]	130.72 ± 7.24	173.85 ± 8.64
E_{dihe}[c]	141.57 ± 12.73	153.68 ± 9.65
E_{impr}	18.64 ± 1.16	27.04 ± 1.02
E_{ele}	−31.90 ± 0.89	−36.22 ± 0.76
rmsd (Å)		
residue numbers	1−14	1−14
backbone	0.17 ± 0.07	0.17 ± 0.08
heavy atoms	0.62 ± 0.21	0.68 ± 0.21
residue numbers	39−48	39−52
backbone	0.16 ± 0.05	0.10 ± 0.04
heavy atoms	1.15 ± 0.24	1.16 ± 0.28
residue numbers	1−14, 39−48	1−14, 39−52
backbone	0.34 ± 0.11	0.29 ± 0.09
heavy atoms	0.99 ± 0.18	1.04 ± 0.20
residue numbers	−3 to 50	−3 to 57
backbone	1.20 ± 0.33	1.18 ± 0.31
heavy atoms	2.03 ± 0.42	2.10 ± 0.40
Ramachandran analysis (%)[d]		
residues in favored region	83.7	83.7
residues in additional allowed regions	9.8	7.9
residues in generously allowed regions	6.2	7.3
residues in disallowed regions	0.3	1.1

[a] None of the structures has distance violations of >0.5 Å and dihedral angle violations of >5°. [b] Two of the long-range distance restraints were derived from the chemical shift changes observed in TM3 residues caused by a single-point mutation (S15Y) in TM2. See Figure S1 in the Supporting Information for details. [c] The final values of square-well NOE and dihedral angle potentials were calculated with force constants of 50 kcal mol^{-1} Å^{-2} and 200 kcal mol^{-1} rad^{-2}, respectively. [d] Ramachandran analysis was performed using PROCHECK-_NMR (*57*). All the residues in the disallowed region are located either in the beginning of the 23 loop or in the C-terminus where the structures are flexible and less defined.

Dynamics of GlyR TM23. The ^{15}N relaxation parameters, R_1 and R_2, and ^{15}N{^{1}H} steady-state heteronuclear NOEs of truncated TM23 were measured at 14.1 and 9.4 T, corresponding to ^{1}H resonances of 600 and 400 MHz, respectively. As shown in Figure 6, most residues have an R_1 value in the range of 0.8−1.2 and 1.6−2.0 s^{-1} at 14.1 and 9.4 T, respectively, and an R_2 value in the range of 15−25 s^{-1} at both field strengths. At 14.1 T, NOE values for most of the residues are above 0.6 from G2 to G17 and from K29 to the C-terminus, except for L35, V37, and L46. At 9.4 T, the NOE values are slightly smaller but the pattern is similar. Both the R_2 and NOE values decrease as one moves toward the N-terminus and the loop region between TM2 and TM3 domains, though the change is rather small. No negative NOE was found under the experimental condition at 30 °C.

Analyzed by the model-free formalism (*32*, *33*), the overall rotational correlation time τ_m was first estimated from the R_2/R_1 ratios using the residue selection criteria outlined by Tjandra (*37*). Those residues whose R_2/R_1 ratios fall outside one standard deviation of the average value and whose NOE

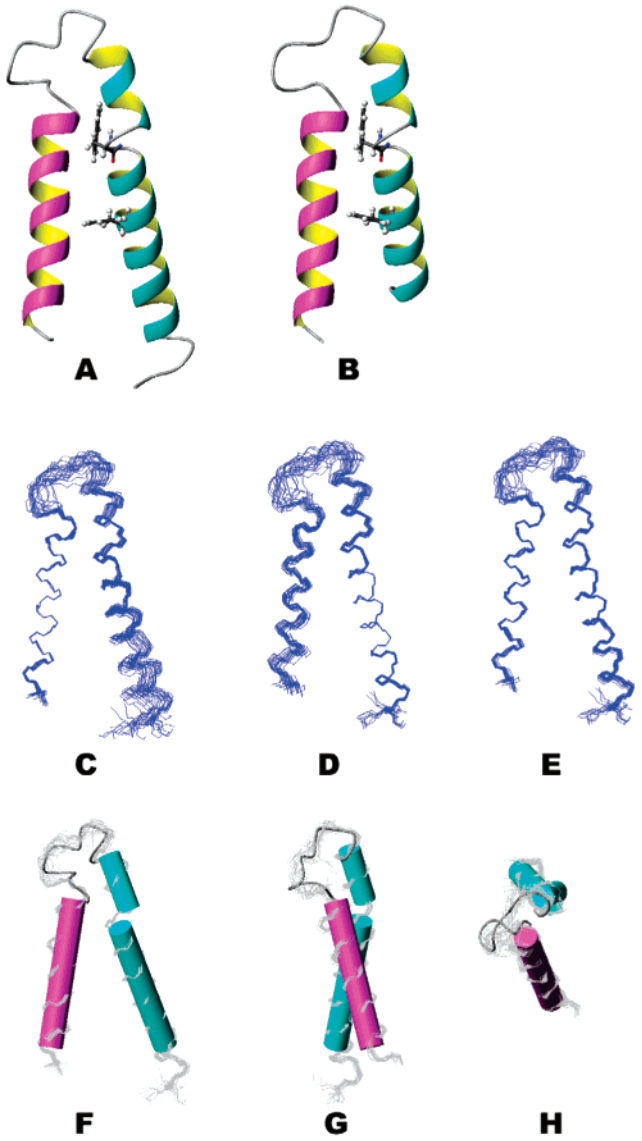

FIGURE 5: Structures of full-length (A) and truncated (B) TM23 segments in TFE are shown in ribbon representation (TM2 in pink and TM3 in cyan). The aromatic side chains of W34 and F41 are depicted in licorice representation, showing that they are situated between the TM2 and TM3 domains instead of facing the solvent. The backbone heavy atoms of the 20 lowest-energy structures were fitted for TM2 alone (C), for TM3 alone (D), and simultaneously for both TM2 and TM3 (E). The cylinder representation shows clearly the kink in the TM3 domain (F and G, side views at two different angles; and H, top view).

values are lower than 0.65 at 14.1 T or lower than 0.55 at 9.4 T were excluded. The initial estimate of the τ_m value for TM23 was 15.9 ns with the data acquired at 9.4 T based on 18 residues, and 14.5 ns with the data at 14.1 T from 21 residues. Further refinement using ModelFree yielded a τ_m value of 14.1 ns. Figure 7 shows the results from the model-free analysis. Most residues in TM23 could be fit well using model 1 (S^2), and some residues were fit better with model 2 (S^2 and τ_e). The S^2 values of the backbone NH groups were in the range of 0.80−0.95 for the residues located in TM2 and TM3 domains and decreased as one moved toward the N-terminus and the 23 loop, indicating relatively higher mobility in these regions.

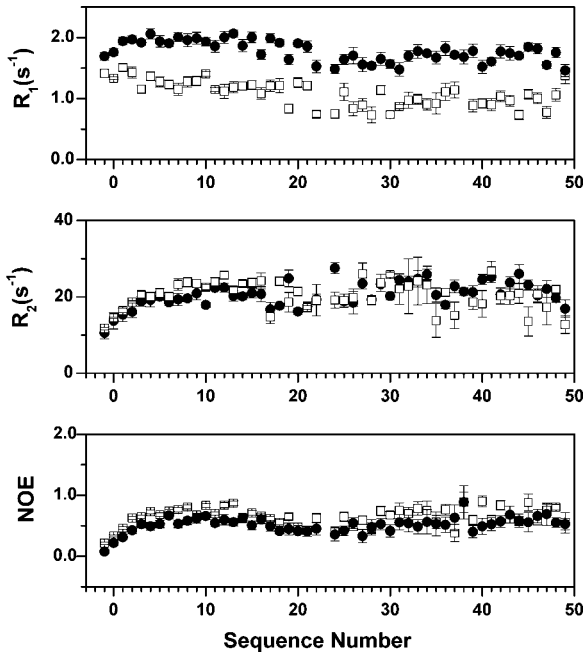

FIGURE 6: Longitudinal and transverse relaxation rate constants, R_1 (A) and R_2 (B), respectively, and $^{15}N\{^1H\}$ NOE (C) of the backbone amide ^{15}N of the truncated TM23 in TFE measured at both 14.1 (□) and 9.4 T (●).

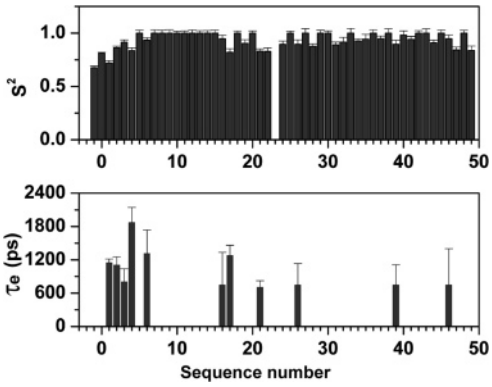

FIGURE 7: Model-free analysis of dynamics of GlyR TM23 in TFE. The dynamics of most residues can be described well by a generalized order parameter (S^2) and an effective correlation time (τ_e), confirming anisotropic (restricted) internal motion and an isotropic overall tumbling for TM23. The τ_m refined by Model-Free is consistent with a monomeric TM23 tumbling in TFE (see the text for details).

DISCUSSION

Validity of the Reductionist Approach by NMR. Large membrane protein assemblies, such as ligand- or voltage-gated receptor channels, are refractory to high-resolution structural determination. Although no single method is perfectly suited for all proteins, complementary advantages of different approaches have made significant progress in recent years. X-ray crystallography remains the preferred method of choice, even though crystallization of membrane proteins proves to be exceedingly difficult and its success is often at the mercy of the leading choices of detergents, which might or might not necessarily mimic the native membrane environment. Binding of a soluble protein, such as an Fv fragment of a monoclonal antibody (*38*, *39*), to membrane proteins to extend their polar regions for cocrystallization of the soluble membrane protein complex is an ingenious

idea, but the generalization of this method assumes that the membrane proteins cocrystallized outside the membrane with the soluble protein retain their native structures in the complex. The substituted cysteine accessibility method (SCAM) has the advantage of working with functional receptor proteins; however, its application is limited to the secondary structures of channel pores, and the negative results are often difficult to interpret (*40*). Moreover, SCAM assumes that cysteine substitution does not change the protein structure, even when channel pharmacology is profoundly altered because of the cysteine substitution. This can potentially be problematic for loops linking two transmembrane domains, where all residues are accessible and the structural information is derived from the reaction rates at different substitution sites. The NMR approach imposes less demand on sample preparation, but spectral crowding and low detection sensitivity limit the size of membrane proteins to be studied. Recent advances in cryo-EM, yielding subnanometer resolution structural templates of membrane proteins, allow high-resolution segmental NMR structures to be pieced together in a reductionist approach (*5*−*7*, *10*, *41*). The central premise of this approach is that the transmembrane domain folding is preprogrammed in the protein sequence such that the secondary helical structure folding in a hydrophobic environment is satisfied by the short-range (intrahelical) interactions whereas the tertiary structural folding is governed by the side chain interactions. This approach has been validated in at least two polytopic TM proteins with known X-ray crystal structures (*9*, *10*), showing excellent agreement between the helix−turn−helix structures determined by NMR in organic solvents and the corresponding motifs in the X-ray structures. The structures determined in this study confirm again that the secondary and tertiary structures of the TM2 and TM3 domains of human GlyR are largely preserved in solvent such as TFE. Indeed, the TM23 structures show distinct domains as expected, including the relatively rigid TM2 and TM3 helices and the more dynamic 23 loop. Thus, it is not unreasonable to infer that certain structural features in TFE partially reflect the TM23 domain structure in the membrane and thus can be used as the first approximation for the future refinement of TM23 structures of the GlyR channel.

Secondary Structural Features of TM2. The residues that span the helical portion of the TM2 domain in the TM23 structures are essentially the same as in the isolated TM2 or the extended TM2 domain previously studied in DPC and TFE (*6*, *7*). We previously showed that merely extending the truncated TM2 domain by four loop residues was enough to ensure the formation of predominantly tetrameric and pentameric oligomers in DPC (*7*). Moreover, because TM2 structures in DPC micelles and DMPG bilayers are very similar (*6*) and because TM2 alone in bilayers can form channels with spontaneous opening having conductance characteristics nearly identical to those of the authentic GlyR channel (*42*, *43*), it is highly likely that the TM2 structure determined in this study resembles the structure of the TM2 domain in the α1-GlyR channel. It is worth noting that the α-helix did not extend beyond S15 in either truncated or extended TM2. We initially attributed this earlier termination of helix to the flexibility near the loose end of the short sequences. In this study, we found that even in the presence of the entire 23 loop and the TM3 domain, the TM2 helix again ended at the same residue, S15, which is the single-point mutation site found to be crucial for GlyR's sensitivity to alcohols and volatile anesthetics. This finding of early termination of α-helix within the TM2 domain is particularly interesting because TFE is known to promote and stabilize the formation of α-helices. Thus, the high-resolution NMR results seem to suggest that the TM2 domain of GlyR is not entirely α-helical and that one-sixth of the TM2 domain near the extracellular interface is intrinsically nonhelical even in a helix-promoting solvent.

This conclusion about the α-helical content in the TM2 domain contrasts with the recent nAChR TM model derived from the 4 Å resolution cryo-EM data (*4*) and a GlyR TM model derived from homology modeling (*44*), both of which assumed a long α-helical structure for the TM2 segment. The models, however, disagree with several lines of key experimental evidence about the secondary structure and helicity in the TM domains of the Cys-loop receptors. For example, Fourier transform infrared (FTIR) spectroscopy of nAChR, after the removal of the extramembrane moieties of the protein, found an α-helix content of only 50% in the TM domains (*11*). Similarly, chemical modification and limited proteolysis coupled with mass spectrometry confirmed that GlyR TM domains could not be entirely α-helical (*12*, *13*). Importantly, CD studies of the reconstitution of homomeric α1-GlyR in phosphatidylcholine vesicles found an α-helix content of only ∼15% (*45*). Since the high-resolution template of the extracellular N-terminal domain of nAChR is now available from the X-ray structure of AChBP, which contains 5.1% α-helix, one can estimate, on the basis of the overall ∼15% α-helix content and the total number of residues in the protein as well as in the extracellular domain and in the TM domains, that the upper limit of α-helical content in the TM domain is ∼50%, in agreement with the FTIR results. The nAChR model derived from the 4 Å cryo-EM data has an exceedingly high helical content, ranging from 83.5% for the β-chain to 87.4% for α- and δ-chains. These values have overestimated the α-helix content in the TM region by 79%, which is equivalent to an at least 168% overestimation of helical content for the entire receptor. In other words, if one accepts both results about the helical content of Cys-loop receptors from the many experimental measurements as well as from the TM2−TM3 portion of the cryo-EM model, then TM1 and TM4 domains combined could only have fewer than eight residues in an α-helical structure and the rest in other nonhelical structures, a prediction that is apparently in disagreement with the pattern of labeling with hydrophobic reagents from the lipids (*46*−*48*). It should also be pointed out that TFE is known to promote α-helix formation and that our TM23 structures determined in TFE probably represent the highest α-helical content possible for these domains. Indeed, the SCAM studies only found ∼75% of the TM2 domain to be α-helical (*2*, *49*, *50*). Thus, it can be concluded that the α-helical content of TM2 is significantly lower than what is assumed in the recent cryo-EM model. The nonhelical extension leading to the 23 loop as shown in our NMR structures might be essential for the flexibility in this region. Such flexibility may prove to be crucial in mediating the TM2 movement during channel gating.

Although the overall secondary structure of the TM2 domain is largely independent of TM3 on the basis of the

comparison of the TM2 structure determined in this study and the structures of isolated TM2 segments, the presence of TM3 nevertheless has a noticeable effect on TM2 because of the tertiary fold of the two domains. In both TM23 and the truncated TM23 structures, the helical portion of TM2 is no longer an ideal helix but slightly curved, with the intrahelical distances being slightly larger on the surface away from the TM3 domain than on the surface facing the TM3 domain. This likely resulted from the stronger intrahelical hydrogen bonding along the hydrophobic surface facing the TM3 domain, as indicated in the periodical change in the H^N chemical shifts from the corresponding random-coil values (Figure 4).

Secondary Structural Features of TM3. The curvature in the TM2 helix, however, is small compared to the discontinuity of the helix in TM3 domain, which exhibits a kink in the vicinity of W34. The existence of a kink in the TM3 domain is evident in the H−D exchange, NOE connectivity, chemical shift, and dynamics data. W34 H^α shows NOE cross-peaks to both V37 H^N and C38 H^N, but the one between W34 H^α and C38 H^N is significantly stronger. The CSI is also different in the region between W34 and V37 compared to that for the nearby residues (Figure 3). Intermediate to fast solvent exchange at D32, A36, and L39 suggests that the intrahelical hydrogen bonding near the kink region is relatively weak. From the calculated structures, it appears that a π-turn or a π-helix is formed from W34 to C38. In the π-helix structure, the $CO\cdots H^N$ hydrogen bond is five instead of four residues apart. Although the π-helix is statistically less favorable than the α-helix or 3_{10}-helix (*51*), a recent study using a slightly modified π-helix definition on 936 nonredundant protein chains with better than 2 Å structural resolution (*52*) revealed that the π-helix occurs significantly more frequently than previously perceived. A detailed analysis of amino acid propensity in forming π-helix suggests that amino acids with bulky side chains, particularly the aromatic ones, are more likely than residues with smaller side chains to be involved in a π-helix (*52*). In general, π-helices are more flexible than α- or 3_{10}-helices. Thus, in TM proteins, a kink with a π-helix or a π-turn might be functionally important. Typically, W and Y residues are more frequently found to be exposed at the lipid−water interface, anchoring TM domains in the lipids. Those that are embedded between TM helices and involved in a π-helix, such as W34 of TM3 in our resolved structure, might play a functional role in providing the conformational flexibility needed for GlyR function. For instance, it has been postulated that the gating of the Cys-loop receptors involves movement of the TM2 domain relative to the rest of the TM architecture (*4*, *6*). Although the loops at two ends of the TM2 domain could act as hinges, the flexibility in the TM3 domain at the W34−C38 kink might also be crucial in accommodating the TM2 movement. Indeed, the dynamics data (R_2 and NOE) showed greater flexibility in the region between W34 and V37 than the rest of the TM3 domain.

Secondary Structural Features of the 23 Loop. There are two Pro residues and four positively charged residues in TM23. They are all located near or in the loop regions. In strict terms, proline at position −2 (P250) belongs to the "12" loop that precedes the TM2 domain. P23 (i.e., P275) is in the middle of the 23 loop. Both proline residues are essential for the turns in the two loops. The four positively charged residues are R0, R19, K24, and K29 (i.e., R252, R271, K276, and K281). R0 and R19 mark the beginning and ending, respectively, of the TM2 domain and are believed to be partially responsible for the GlyR channel selectivity for the anions. The positive charges of the K24 side chain in the 23 loop region may also contribute to the overall electrostatic interaction favoring negatively charged Cl^- near the extracellular entrance of the GlyR channel. An interesting finding is that the dynamics profile in the 23 loop is not uniform. It seems that the last three residues of TM2 (SGS) and the first eight residues of the 23 loop (RASLPKVS) are less structured and more flexible than the remainder of the 23 loop, where the last six residues form a helical structure. Our preliminary homology modeling and docking study based on the X-ray structure of AChBP for the extracellular domain and the TM23 structure from this study suggest that the NFPMDVQ sequence in the Cys loop is adjacent to the SLPKVS sequence in the 23 loop, with P146 and P275 marking the opposing tip of the respective loops (unpublished observation). Because of the dynamic nature of the flexible moiety of the 23 loop and the possible movement of the two adjacent loops relative to each other, several favorable interactions can occur, including the salt bridge between D148 and K276, the hydrophobic interactions between F145 and L274 and between V149 and V277, and the side chain hydrogen bonding between N144 and S273 and between Q150 and S278. Some or all of these interactions may prove to be crucial to the coupling between the agonist binding in the extracellular domain and the movement of the TM2 domain in the event of channel gating.

Tertiary Structural Features. One of the major difficulties in the structural determination of multidomain TM proteins is the lack of long-range distance restraints. Even with recently proposed residual dipole coupling measurements for orientational restraints using magnetically or mechanically aligned samples (*53*), high-resolution tertiary (and quaternary) structural information is still scarce, particularly because some TM domain residues are not entirely NMR visible in the lipid environment due to slow conformation exchange. Thus, measuring multidomain TM structures in TFE has the advantage of achieving a sufficiently high resolution to yield long-range NOE connectivity. For TM23, several pairs of long-range NOEs were positively identified. These are mainly from the side chain to backbone interactions and side chain to side chain interactions derived from 2D NOESY spectra. Fortunately, the aromatic side chain resonances from W34 and F41 are well-resolved, and their long-range NOE cross-peaks with the TM2 domain can be assigned unambiguously, defining the tertiary fold of TM3 relative to TM2. It should be noted that once the helical structures of the two domains are determined by the short and midrange NOEs, only a few long-range NOEs are needed to define the tertiary fold.

The left-handed tilt of TM3 relative to TM2 found in TFE is very likely preserved in the authentic GlyR channel structure. This is true because the high-resolution TM2 structures (*6*, *19*) showed that the hydrophilic residues, which likely line the pore, are not aligned parallel to the long axis of the TM2 helix, but rather at an ∼14° angle. To align these pore-lining hydrophilic residues parallel to the channel axis, the axes of the TM2 helices in the pentameric channel assembly must tilt in a right-handed fashion. The left-handed

FIGURE 8: Built upon the monomeric NMR structure of TM2 (pink) and TM3 (cyan) from our study, a homopentameric model of the pore architecture of human glycine receptor is optimized by extensive energy minimization and >1 ns all-atom NPT simulations in a fully hydrated POPC membrane. The first transmembrane domain (gray) was generated by homology modeling and attached to TM2 only to show its possible location relative to TM23 in a channel complex.

tilt of TM3 relative to TM2 then ensures that the TM3 axis is more or less in the transmembrane direction. If the TM3 tilt were right-handed relative to TM2 and five TM2 domains must form a right-handed channel pore, then TM3 would probably not be long enough to traverse the lipid bilayer. As shown in Figure 8, a left-handed tertiary tilt between TM2 and TM3 and a right-handed quaternary tilt of five subunits can yield a neatly packed channel assembly.

Backbone Dynamics. The backbone dynamics measurements provided further support to the structural features discussed above. The dynamics of TM23 segments (Figures 6 and 7) clearly shows distinct domain structures as marked by relatively rigid TM2 and TM3 helices and the relatively flexible 23 loop. The discontinuity of the TM3 helix near the kink region is also clearly discernible in the R_2 and NOE profiles. It is rather remarkable that the difference in the motional characteristics of the TM domains and the loop is preserved even in TFE, where unlike in the membrane, the separation of the hydrophobic phase for the TM domain and aqueous phase for the loop is absent. Hence, the dynamics data also support the notion that as long as the segments are properly truncated, the domain structures are predetermined by the sequence and proper solvent environment.

The model-free analysis employed in this study assumes anisotropic (restricted) internal motion and an isotropic overall tumbling for the peptide. This assumption seems reasonable for TM23 in TFE because the dynamics of most residues can be described well by a generalized order parameter (S^2) and an effective correlation time (τ_e). The measured overall tumbling rate ($\tau_m \sim 14$ ns) is consistent with a monomeric TM23 (~8−9 kDa) in TFE. Compared to that of a protein in water, the tumbling in TFE is expected to be 2−3 times slower because the viscosity of TFE is twice that of water (*54*). Assuming everything else is equal, a factor of 2 increase in the viscosity of the solvent will typically result in a ~2−3-fold increase in τ_m (*55*, *56*). Although there is a slight possibility that nonspecific or transient association of TM23 could occur at 1.7 mM in TFE, such association (if any) should not contribute significantly to τ_m because no residues showed evidence of exchange (Figure 7). This dynamics confirmation of monomeric TM23 in TFE is important because it validates that the long-range NOEs indeed belong to the intrasubunit instead of intersubunit restraints.

Met → Leu Mutations. To avoid CNBr cleavage at two internal Met sites (M11 and M35) during the separation of the expressed TM23 from the fusion protein, the common practice of mutating Met to Leu was implemented. These mutations are trivial and presumably better tolerated than many cysteine substitution mutations. Hence, they are not expected to have major structural consequences. This is confirmed by comparing the high-resolution NMR structures of the expressed TM2 having the M11L mutation (*7*) to the high-resolution NMR structures of the synthesized TM2 with the wild-type sequence (*6*). The high-resolution structures are essentially identical within the segment containing the mutation. Moreover, Leu is actually at both positions in the wild-type sequence of the β-form of GlyR. It should be noted that both homomeric α1-GlyR and heteromeric α1-β-GlyR form functional receptors, with the former being mostly in young animals and selected regions in the adults and the latter being predominantly in the adults. Thus, major conclusions of this study will not change due to the M to L mutations.

In conclusion, we have in this study determined the high-resolution NMR structure of TM23 domains of the human glycine receptor α1 subunit. This is the first time that two TM domains of a Cys-loop receptor, linked by the important 23 loop, have ever been characterized at atomistic resolution. We recognize that the TM23 structure in TFE might not be fully representative of the structure in a glycine receptor. The structural and dynamical features that can be distinguished as the stable TM domains jointed by the flexible 23 loop in TFE nevertheless suggest that many structural characteristics of the receptor can be inferred from this study. Most importantly, in the helix-promoting medium of TFE, the TM2 domain is not entirely helical but rather has a relatively short helix ending at the same residue as in the TM2 structure determined in DPC micelles. This result raises questions about the exceedingly high helical content in a recent model of nAChR, which seems to disagree with many experimental data, including those presented here. Moreover, the kink in the TM3 domain as well as the different dynamics behaviors of the first half from the second half of the putative loop region has never been reported before. It is also evident that the tertiary structure of the two domains has a left-handed arrangement. This arrangement seems to be necessary to ensure a right-handed quaternary packing of five subunits to form an ion-conducting channel in the glycine receptor.

ACKNOWLEDGMENT

We thank Dr. Michael Cascio for providing the cDNA of the α1 subunit of human glycine receptor and Drs. Jun Qin and Xi-an Mao for arranging the use of a NMR spectrometer at the Cleveland Clinic. The participation by Dr. Pravat Mandal in the initial NMR data acquisition and processing is acknowledged.

SUPPORTING INFORMATION AVAILABLE

Long-range distance restraints derived from the chemical shift changes (Figure S1). This material is available free of charge via the Internet at http://pubs.acs.org.

REFERENCES

1. Kao, P. N., Dwork, A. J., Kaldany, R. R., Silver, M. L., Wideman, J., Stein, S., and Karlin, A. (1984) Identification of the α subunit half-cystine specifically labeled by an affinity reagent for the acetylcholine receptor binding site, *J. Biol. Chem. 259*, 11662−11665.
2. Karlin, A. (2002) Emerging structure of the nicotinic acetylcholine receptors, *Nat. Rev. Neurosci. 3*, 102−114.
3. Brejc, K., van Dijk, W. J., Klaassen, R. V., Schuurmans, M., van Der Oost, J., Smit, A. B., and Sixma, T. K. (2001) Crystal structure of an ACh-binding protein reveals the ligand-binding domain of nicotinic receptors, *Nature 411*, 269−276.
4. Miyazawa, A., Fujiyoshi, Y., and Unwin, N. (2003) Structure and gating mechanism of the acetylcholine receptor pore, *Nature 424*, 949−955.
5. Opella, S. J., Marassi, F. M., Gesell, J. J., Valente, A. P., Kim, Y., Oblatt-Montal, M., and Montal, M. (1999) Structures of the M2 channel-lining segments from nicotinic acetylcholine and NMDA receptors by NMR spectroscopy, *Nat. Struct. Biol. 6*, 374−379.
6. Tang, P., Mandal, P. K., and Xu, Y. (2002) NMR structures of the second transmembrane domain of the human glycine receptor α_1 subunit: Model of pore architecture and channel gating, *Biophys. J. 83*, 252−262.
7. Yushmanov, V. E., Mandal, P. K., Liu, Z., Tang, P., and Xu, Y. (2003) NMR structure and backbone dynamics of the extended second transmembrane domain of the human neuronal glycine receptor α1 subunit, *Biochemistry 42*, 3989−3995.
8. Popot, J. L., and Engelman, D. M. (1990) Membrane protein folding and oligomerization: The two-stage model, *Biochemistry 29*, 4031−4037.
9. Bennett, M., Yeagle, J. A., Maciejewski, M., Ocampo, J., and Yeagle, P. L. (2004) Stability of loops in the structure of lactose permease, *Biochemistry 43*, 12829−12837.
10. Katragadda, M., Alderfer, J. L., and Yeagle, P. L. (2001) Assembly of a polytopic membrane protein structure from the solution structures of overlapping peptide fragments of bacteriorhodopsin, *Biophys. J. 81*, 1029−1036.
11. Gorne-Tschelnokow, U., Strecker, A., Kaduk, C., Naumann, D., and Hucho, F. (1994) The transmembrane domains of the nicotinic acetylcholine receptor contain α-helical and β structures, *EMBO J. 13*, 338−341.
12. Leite, J. F., and Cascio, M. (2002) Probing the topology of the glycine receptor by chemical modification coupled to mass spectrometry, *Biochemistry 41*, 6140−6148.
13. Leite, J. F., Amoscato, A. A., and Cascio, M. (2000) Coupled proteolytic and mass spectrometry studies indicate a novel topology for the glycine receptor, *J. Biol. Chem. 275*, 13683−13689.
14. Cascio, M. (2004) Structure and function of the glycine receptor and related nicotinicoid receptors, *J. Biol. Chem. 279*, 19383−19386.
15. Skopp, R. N., and Lane, L. C. (1988) Fingerprinting of proteins cleaved in solution by cyanogen bromide, *Appl. Theor. Electrophor. 1*, 61−64.
16. Mihic, S. J., Ye, Q., Wick, M. J., Koltchine, V. V., Krasowski, M. D., Finn, S. E., Mascia, M. P., Valenzuela, C. F., Hanson, K. K., Greenblatt, E. P., Harris, R. A., and Harrison, N. L. (1997) Sites of alcohol and volatile anaesthetic action on GABA(A) and glycine receptors, *Nature 389*, 385−389.
17. Miller, C. (1989) Genetic manipulation of ion channels: A new approach to structure and mechanism, *Neuron 2*, 1195−1205.
18. Lobley, A., Whitmore, L., and Wallace, B. A. (2002) DICHROWEB: An interactive website for the analysis of protein secondary structure from circular dichroism spectra, *Bioinformatics 18*, 211−212.
19. Yushmanov, V. E., Xu, Y., and Tang, P. (2003) NMR structure and dynamics of the second transmembrane domain of the neuronal acetylcholine receptor β2 subunit, *Biochemistry 42*, 13058−13065.
20. Piotto, M., Saudek, V., and Sklenar, V. (1992) Gradient-tailored excitation for single-quantum NMR spectroscopy of aqueous solutions, *J. Biomol. NMR 2*, 661−665.
21. Marion, D., and Wuthrich, K. (1983) Application of phase sensitive two-dimensional correlated spectroscopy (COSY) for measurements of ^{1}H−^{1}H spin−spin coupling constants in proteins, *Biochem. Biophys. Res. Commun. 113*, 967−974.
22. Wishart, D. S., Bigam, C. G., Yao, J., Abildgaard, F., Dyson, H. J., Oldfield, E., Markley, J. L., and Sykes, B. D. (1995) ^{1}H, ^{13}C and ^{15}N chemical shift referencing in biomolecular NMR, *J. Biomol. NMR 6*, 135−140.
23. Farrow, N. A., Muhandiram, R., Singer, A. U., Pascal, S. M., Kay, C. M., Gish, G., Shoelson, S. E., Pawson, T., Forman-Kay, J. D., and Kay, L. E. (1994) Backbone dynamics of a free and phosphopeptide-complexed Src homology 2 domain studied by ^{15}N NMR relaxation, *Biochemistry 33*, 5984−6003.
24. Delaglio, F., Grzesiek, S., Vuister, G. W., Zhu, G., Pfeifer, J., and Bax, A. (1995) NMRPipe: A multidimensional spectral processing system based on UNIX pipes, *J. Biomol. NMR 6*, 277−293.
25. Garrett, D. S., Powers, R., Gronenborn, A. M., and Clore, G. M. (1991) *J. Magn. Reson. 95*, 214−220.
26. Goddard, T. D., and Kneller, D. G. (2002) *Sparky*, University of California, San Francisco.
27. Schwieters, C. D., Kuszewski, J. J., Tjandra, N., and Clore, G. M. (2003) The Xplor-NIH NMR molecular structure determination package, *J. Magn. Reson. 160*, 65−73.
28. Brünger, A. T. (1992) *X-PLOR-NIH*, Yale University Press, New Haven, CT.
29. Nilges, M., Clore, G. M., and Gronenborn, A. M. (1988) Determination of three-dimensional structures of proteins from interproton distance data by dynamical simulated annealing from a random array of atoms. Circumventing problems associated with folding, *FEBS Lett. 239*, 129−136.
30. Sorgen, P. L., Cahill, S. M., Krueger-Koplin, R. D., Krueger-Koplin, S. T., Schenck, C. C., and Girvin, M. E. (2002) Structure of the *Rhodobacter sphaeroides* light-harvesting 1β subunit in detergent micelles, *Biochemistry 41*, 31−41.
31. Lobo, I. A., Trudell, J. R., and Harris, R. A. (2004) Cross-linking of glycine receptor transmembrane segments two and three alters coupling of ligand binding with channel opening, *J. Neurochem. 90*, 962−969.
32. Lipari, G., and Szabo, A. (1982) Model-Free Approach to the Interpretation of Nuclear Magnetic Resonance Relaxation in Macromolecules. 1. Theory and Range of Validity, *J. Am. Chem. Soc. 104*, 4546−4559.
33. Lipari, G., and Szabo, A. (1982) Model-Free Approach to the Interpretation of Nuclear Magnetic Resonance Relaxation in Macromolecules. 2. Analysis of Experimental Results, *J. Am. Chem. Soc. 104*, 4559−4570.
34. Mandel, A. M., Akke, M., and Palmer, A. G., III (1995) Backbone dynamics of *Escherichia coli* ribonuclease HI: Correlations with structure and function in an active enzyme, *J. Mol. Biol. 246*, 144−163.
35. Kay, L. E., Torchia, D. A., and Bax, A. (1989) Backbone dynamics of proteins as studied by ^{15}N inverse detected heteronuclear NMR spectroscopy: Application to staphylococcal nuclease, *Biochemistry 28*, 8972−8979.
36. Wishart, D. S., Sykes, B. D., and Richards, F. M. (1992) The chemical shift index: A fast and simple method for the assignment of protein secondary structure through NMR spectroscopy, *Biochemistry 31*, 1647−1651.
37. Tjandra, N., Kuboniwa, H., Ren, H., and Bax, A. (1995) Rotational dynamics of calcium-free calmodulin studied by ^{15}N NMR relaxation measurements, *Eur. J. Biochem. 230*, 1014−1024.
38. Iwata, S., Ostermeier, C., Ludwig, B., and Michel, H. (1995) Structure at 2.8 Å resolution of cytochrome *c* oxidase from *Paracoccus denitrificans*, *Nature 376*, 660−669.
39. Ostermeier, C., and Michel, H. (1997) Crystallization of membrane proteins, *Curr. Opin. Struct. Biol. 7*, 697−701.
40. Lynch, J. W. (2004) Molecular structure and function of the glycine receptor chloride channel, *Physiol. Rev. 84*, 1051−1095.
41. Yeagle, P. L., and Albert, A. D. (2002) Use of nuclear magnetic resonance to study the three-dimensional structure of rhodopsin, *Methods Enzymol. 343*, 223−231.
42. Marsh, D. (1996) Peptide models for membrane channels, *Biochem. J. 315*, 345−361.
43. Reddy, G. L., Iwamoto, T., Tomich, J. M., and Montal, M. (1993) Synthetic peptides and four-helix bundle proteins as model systems

for the pore-forming structure of channel proteins. II. Transmembrane segment M2 of the brain glycine receptor is a plausible candidate for the pore-lining structure, *J. Biol. Chem. 268*, 14608−14615.
44. Mascia, M. P., Trudell, J. R., and Harris, R. A. (2000) Specific binding sites for alcohols and anesthetics on ligand-gated ion channels, *Proc. Natl. Acad. Sci. U.S.A. 97*, 9305−9310.
45. Cascio, M., Shenkel, S., Grodzicki, R. L., Sigworth, F. J., and Fox, R. O. (2001) Functional reconstitution and characterization of recombinant human α1-glycine receptors, *J. Biol. Chem. 276*, 20981−20988.
46. Blanton, M. P., Dangott, L. J., Raja, S. K., Lala, A. K., and Cohen, J. B. (1998) Probing the structure of the nicotinic acetylcholine receptor ion channel with the uncharged photoactivable compound 3H-diazofluorene, *J. Biol. Chem. 273*, 8659−8668.
47. Blanton, M. P., and Cohen, J. B. (1994) Identifying the lipid−protein interface of the *Torpedo* nicotinic acetylcholine receptor: Secondary structure implications, *Biochemistry 33*, 2859−2872.
48. Blanton, M. P., and Cohen, J. B. (1992) Mapping the lipid-exposed regions in the *Torpedo californica* nicotinic acetylcholine receptor, *Biochemistry 31*, 3738−3750.
49. Akabas, M. H., Kaufmann, C., Archdeacon, P., and Karlin, A. (1994) Identification of acetylcholine receptor channel-lining residues in the entire M2 segment of the α subunit, *Neuron 13*, 919−927.
50. Zhang, H., and Karlin, A. (1998) Contribution of the β subunit M2 segment to the ion-conducting pathway of the acetylcholine receptor, *Biochemistry 37*, 7952−7964.
51. Rohl, C. A., and Doig, A. J. (1996) Models for the 3_{10}-helix/coil, π-helix/coil, and α-helix/3_{10}-helix/coil transitions in isolated peptides, *Protein Sci. 5*, 1687−1696.
52. Fodje, M. N., and Al-Karadaghi, S. (2002) Occurrence, conformational features and amino acid propensities for the π-helix, *Protein Eng. 15*, 353−358.
53. Mesleh, M. F., Lee, S., Veglia, G., Thiriot, D. S., Marassi, F. M., and Opella, S. J. (2003) Dipolar waves map the structure and topology of helices in membrane proteins, *J. Am. Chem. Soc. 125*, 8928−8935.
54. Gente, G., and La Mesa, C. (2000) Water-trifluoroethanol mixtures: Some physicochemical properties, *J. Solution Chem. 29*, 1159−1172.
55. Lee, L. K., Rance, M., Chazin, W. J., and Palmer, A. G., III (1997) Rotational diffusion anisotropy of proteins from simultaneous analysis of ^{15}N and $^{13}C^{\alpha}$ nuclear spin relaxation, *J. Biomol. NMR 9*, 287−298.
56. Gustavsson, T., Cassara, L., Marguet, S., Gurzadyan, G., van der Meulen, P., Pommeret, S., and Mialocq, J. C. (2003) Rotational diffusion of the 7-diethylamino-4-methylcoumarin C1 dye molecule in polar protic and aprotic solvents, *Photochem. Photobiol. Sci. 2*, 329−341.
57. Laskowski, R. A., Rullmannn, J. A., MacArthur, M. W., Kaptein, R., and Thornton, J. M. (1996) AQUA and PROCHECK-NMR: Programs for checking the quality of protein structures solved by NMR, *J. Biomol. NMR 8*, 477−486.

BI050256N